Measurement 247 (2025) 116765

Contents lists available at ScienceDirect

Measurement

journal homepage: www.elsevier.com/locate/measurement

Bio-inspired 3D-printed phantom: Encoding cellular heterogeneity for characterization of quantitative phase imaging

Sylvia Desissaire [a], Michał Ziemczonok [b], Tigrane Cantat-Moltrecht [a], Arkadiusz Kuś [b], Guillaume Godefroy [a], Lionel Hervé [a], Chiara Paviolo [a], Wojciech Krauze [b], Cédric Allier [a,c], Ondrej Mandula [a,*], Małgorzata Kujawińska [b,*]

[a] Univ. Grenoble Alpes, CEA Leti, 17 av. des Martyrs, Grenoble, F-38000, France
[b] Warsaw University of Technology, Institute of Micromechanics and Photonics, Boboli 8 Street, Warsaw, 02-525, Poland
[c] Janelia Research Campus, Howard Hughes Medical Institute, 19700 Helix Dr, Ashburn, VA, USA

ARTICLE INFO

Keywords:
Quantitative phase imaging
Phase calibration target
Cell phantom
Two-photon polymerization lithography
Metrology
Inter-laboratory comparison

ABSTRACT

Quantitative phase imaging (QPI) has proven to be a valuable tool for advanced biological and pharmacological research, providing phase information for the study of cell features and physiology in label-free conditions. The next step for QPI to become a gold standard is the quantitative assessment of the phase gradients over the different microscopy setups. Given the large variety of QPI systems, a systematic comparison is a challenging task, and requires a calibration target representative of the living samples. In this paper, we introduce a tailor-made 3D-printed phantom derived from phase images of eukaryotic cells. It comprises typical morphologies and optical thicknesses found in biological cultures and is characterized with digital holographic microscopy (reference measurements). The performance of three different full field QPI optical systems, in terms of optical path difference and dry mass accuracy, were evaluated. This phantom opens up other possibilities for the validation of reconstruction algorithms and post-processing routines, and paves the way for calibration targets designed *ad hoc* for specific biological questions.

1. Introduction

Quantitative phase imaging (QPI) is a label-free microscopy approach providing quantitative maps of optical path length delays introduced by a specimen [1]. Even though the fundamentals of this technique have been known for almost a century [2], QPI has developed dramatically over the last 10–15 years thanks to the technological progresses of imaging sensors and increase in computer power [3]. QPI is now transitioning to many biomedical laboratories as valuable technique for measuring fundamental cellular properties including cell dry mass and growth rate [4–6], viscoelastic properties [7,8], cell migration [9], and intracellular transport [10]. Despite these advances, the field is still lacking systematic comparisons between instruments, phase reconstruction methods, acquisition protocols, and image post-processing algorithms. This evaluation is of paramount importance to draw biological conclusions based on QPI measurements [11,12].

At present, the gold standard for calibration is the USAF test chart [13,14]. These standards are typically made of thin metal films, which are mainly adapted for quantifying the spatial resolution in absorption and do not function as pure phase objects [15]. There are bar or spoke charts adapted for phase contrast [16,17], however, they are typically measured in air, which create distinct measurement conditions, sharp edges and high refractive index (RI) contrasts not related to biological samples. Polystyrene beads can also be used as calibration objects for different QPI methods [14,18], however, the typically large refractive index difference between polystyrene (RI ≈ 1.59 at 632 nm wavelength) and cell culture media (RI ≈ 1.33), which can lead to phase unwrapping artifacts together with the round shape of the beads, which is too simple, means they cannot be considered as good representation of biological samples [15]. Phase calibration can also be achieved with biological objects of known dry mass variation. As an example, mouse red blood cells could serve as an informative standard because of the established average cell mass range, but they cannot be a calibration tool [19–21]. Recently, 3D-printing techniques have been used to create phantoms for a wide range of imaging instruments [22–26], including structures featuring refractive index and dimensional properties typically found in mammalian cells [27]. These micro-phantoms hold great potential to standardize the characterization of QPI systems, however, they lack the typical biological morphologies seen in complex biological models.

* Corresponding authors.
E-mail addresses: ondrej.mandula@cea.fr (O. Mandula), malgorzata.kujawinska@pw.edu.pl (M. Kujawińska).

https://doi.org/10.1016/j.measurement.2025.116765
Received 23 September 2024; Received in revised form 11 December 2024; Accepted 14 January 2025
Available online 22 January 2025

We propose here a novel 3D-printed micro-phantom to assess the metrological performance of QPI systems for biological experiments. The phantom has been conceived with phase images of eukaryotic cells (HeLa cells) acquired with digital holographic microscopy (DHM). The target was designed to encode typical cellular heterogeneity as captured on 2D systems, namely morphology and optical thickness, while ensuring that the range of values and measurement conditions match the biological experiments. This approach offers the opportunity to tailor the phantom to the particular biological task, as well as test automatic data processing routines to ascertain their influence on the measured features. We demonstrate how the phantom can be used as a calibration standard for different QPI methods: quadri-wave lateral shearing interferometer (QWLSI) [28], lensfree microscopy (LFM) [29], and defocused microscopy (DFM) [30].

2. 2D cell phantom

2.1. Scope and motivation

For QPI techniques to become commonly used in biological research, the reliability of their results and their acceptance by the scientific community should be ensured. Best practices, as reported for fluorescence microscopy [31], are essential to ensure reproducibility and accurate data interpretation. To that aim, metrics, such as accuracy and repeatability could be retrieved using calibrated phantoms made *ad hoc* for the specific application. Taking into account the diversity of biological research, which may e.g. focus on the study of individual cells, cell cultures, tissue slices or 3D organoids of different organs, design a unique phantom would be impractical. Even within single cell lines and sparse cultures, the diverse cell features (e.g. nucleus, organelles) can show different morphological details, thus impacting the phase information of the studied phenomenon. We thus propose that the phantom should be designed upstream, according to the targeted application. At the scale of an individual study, it may guide the choice toward the best suited QPI method available and set its scope of application. For inter laboratory comparison, it may provide a robust tool to quantify errors and evaluate the reproducibility of results over different measurement campaigns.

Our study focuses on the comparison of full field QPI techniques for imaging of adherent cells with morphological heterogeneity, namely QWLSI, LFM, and DFM. Results from these techniques have been compared to the respective DHM reference. An overview of the system specifications is given in Table 1 (for detailed description, see Methods 5.2). While methods such as DHM and QWLSI provide high spatial resolution, particularly interesting to investigate small changes at the individual cell level, DFM and LFM large fields of view (FOV) facilitate the imaging of a cell culture over time. These techniques operating rather differently, the designed phantom should allow the independent evaluation of several parameters, both qualitatively and quantitatively, in an easy manner. Here we focus on the optical path difference (OPD) in each (x,y) position within the cell as well as the cell dry mass obtained by integrating the OPD values over the entire projected cell area, as detailed in Section 5.3. These are common parameters retrieved from QPI measurements, which should be determined with accuracy to validate statistical analysis on large biological samples. The range of OPD and dry mass values covered by the phantom should be set according to the state of the art related to the biological application. Cells of various shapes and areas should be included in order to investigate the impact of such morphological heterogeneity on the accuracy of the phase retrieval. In principle the utility of the phantom can be expanded to incorporate additional sample variabilities such as cell confluence, multilayered culture or internal refractive index variability.

Table 1
QPI systems main specifications.

System	FOV (μm²)	Wavelength (nm)
Digital holographic microscope	120 × 120	632
Quadri-wave lateral shearing interferometer	596 × 504	530
Defocused microscope	2364 × 1586	450
Lensfree microscope	6413 × 4542	450, 540, 630

2.2. Phantom design

The phantom presented in this work has been developed based on 16 measurements of adherent HeLa cells imaged with a DHM. This initial measurement needs to contain essential phase and morphological details that will be used for inferring the targeted biomedical information. Cells have been segmented by hand to represent different shapes and sizes. The original phase maps were then adjusted to cover larger range of OPD and phase variability profile, and finally assembled in 22 test groups (for a total of 176 cells) divided in three main fields (see Fig. 1(a) for details and supplementary Fig. A.1 for the complete phantom design):

- Field 1 – OPD accuracy with respect to the cell shape. The field consists of flat cells at approximately 100 nm OPD, obtained from the segmented masks from all 16 cells. Their area ranges from 100 to 1100 μm².
- Field 2 – OPD accuracy with respect to the OPD value. The field consists of 16 groups of 5 flat cells (80 cells in total). The average OPD per group is ranging from 10 to 416 nm. The selected cells have different shapes and similar OPD value within each group.
- Field 3 – dry mass accuracy with respect to the OPD profile and the cell shape. This field has 5 groups of 16 cells (same area masks as field 1) each with variable height (phase) profiles (80 cells in total). The average dry mass of cells in each group is ranging from 61 pg ([min, max]=[11,136] pg) to 521 pg ([min, max]=[59, 1257] pg).

These profiles were then printed with a 3D lithography system on a standard glass coverslip (details given in Section 5.1).

3. Results

3.1. Experimental procedure

In most QPI systems it is assumed that the complex field is a good representation of the measured object. This is only true if the object is in focus and does not exceed the depth of field. Large depth of focus requires low NA and therefore low spatial resolution. The proposed DHM system (in laboratory 1) utilizes optical diffraction tomography hardware setup and additional processing steps for integrated phase measurements (see Methods 5.2.1). As a result, it overcomes limitations mentioned above and provides both high resolution, extended depth of field and interferometric accuracy of the phase. In this study, such DHM results are treated as reference values for the validation of the three other full field methods (QWLSI, DFM, LFM: in laboratory 2). The percent error (PE), calculated as defined in Section 5.4, is used as metric for quantifying OPD accuracy in fields 1 and 2 and dry mass accuracy in field 3, with respect to DHM results. OPD and dry mass in each cell are retrieved applying the same post-processing pipeline to the reconstructed OPD (phase) maps of all systems. It includes cell segmentation on the theoretical mask and additional post-processing steps, as described in Section 5.3. Direct comparison of the different hardware and phase reconstruction software can this way be emphasized.

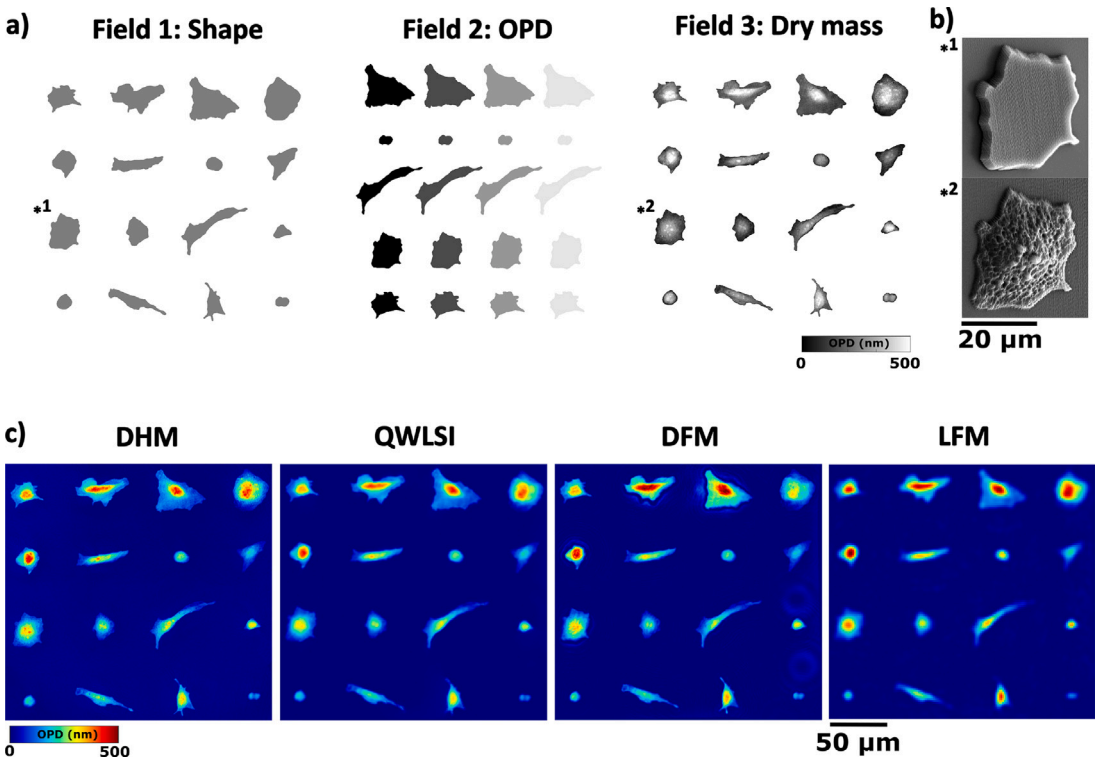

Fig. 1. Overview of the cell phantom design. It consists of three fields as shown in (a), where field 1 and field 2 only include flat cells (constant OPD profile) and field 3 only cells with variable height profiles (non constant OPD profile). (b) Scanning electron microscopy images of a single cell printed with both of these profiles (*1 flat, *2 variable height). Field 1 is made of 16 different cells with approximately same OPD value to test OPD accuracy with respect to shape. Field 2 consists of 16 groups (only 4 groups shown here) of 5 different cells with increasing OPD value to test OPD accuracy with respect to OPD. Field 3 consists of 5 groups (only one group shown here) of 16 different cells with increasing dry mass values to test dry mass accuracy with respect to shape and OPD. The full printed phantom is given in supplementary Fig. A.1. (c) Images from field 3 (group 4) acquired with each modality.

3.2. Field 1: OPD accuracy with respect to cell shape

OPD accuracy and precision were estimated for each flat cell of field 1 (as defined in Fig. 1(a)). Their mean OPD values, as measured with DHM, range from 60 nm to 109 nm. In Fig. 2(a), the PE obtained for each cell (bars) is given along with the relative standard deviation (RSD) within each cell (errobars). High accuracy is achieved using QWLSI, with the PE ranging from −7% to 4% and a mean RSD (over the 16 cells) of 6%. This last value is similar to the one obtained for the ground truth, i.e. mean RSD of 7% and individual value per cell given by the dashed line on Fig. 2(a). Qualitatively, these results correspond to an overall good homogeneity in the cell phase maps, independently of the cell shape, as shown in Fig. 2(b). LFM and DFM are less reliable when imaging such flat cells. Mean OPD values appears to generally be overestimated in DFM, with PE ranging from −3% to 58%, while they are always underestimated in LFM, with PE ranging from −27% to −4%. Phase homogeneity is lost in some cells measured with both of these techniques as shown in the maps, which is consistent with the higher mean RSD of 21% and 10% calculated for LFM and DFM, respectively. The lack of fidelity of the reconstruction can be explained by the lack of signal content in the measurement. Indeed, diffraction intensity measurement is not sensitive to low frequency components of the OPD, such as in those flat cells. This can also be explained by the fact that the image reconstruction algorithms were fine tuned for real experimental conditions, i.e. with cells of variable height profiles rather than flat cells. Elongated cells seem to generally exhibit such non-homogeneous phase distribution. These deviations may, however, be seen in cells of other shapes, without a clear pattern. Overall, no clear dependence between cell shape (e.g. based on area or eccentricity) and OPD precision and accuracy can therefore be claimed from these results. The phase maps of all 16 cells are given in supplementary material, Fig. A.2.

3.3. Field 2: OPD accuracy with respect to OPD value

Measurement accuracy depending on OPD was then evaluated in field 2 (as defined in Fig. 1(a)). For each group of this field (consisting of 5 flat cells of different shape), the mean OPD value was progressively increased from 10 nm to 416 nm. The PE per cell was calculated using Eq. (3). Fig. 3(a) summarizes the results as mean PE within each group (data points) along with the SD of the PE within each group (shaded area). For all tested modalities, the PE is within 30% when the cell OPD ranges from 50 nm to 300 nm. In the case of QWLSI, OPD values are overall slightly underestimated as compared to the reference (PE ≈ 5%–10%) and high precision is achieved over this entire range (SD ≈ 4%). LFM best accuracy is obtained for cells with OPD from 200 nm to 300 nm (PE< 6% with SD ≈ 6%). For thinner cells, the accuracy drops and OPD values are underestimated by around 20%. In the case of DFM, the mean error is around 10% in the OPD range of 50–300 nm, however, comparatively large shaded area reveals much lower precision that the other systems (SD up to ≈ 20%). The phase maps of a cell at different OPD values, given in Fig. 3(b), underline these differences between systems. The inhomogeneity in the phase maps seems generally larger in DFM, independently of the OPD value. For low OPD values (< 40 nm), the cell phase cannot be properly differentiated from the noise level anymore and the obtained results cannot be exploited directly, in particular using LFM and DFM. At high OPD values (> 300 nm) the reconstructions for QWLSI and DFM dropped in accuracy, while LFM failed to retrieve the cell shape due to phase wrapping errors.

3.4. Field 3: Dry mass accuracy with respect to variable OPD profiles

In experimental conditions, the biological cells under evaluation commonly have variable height profiles rather than flat ones. In such

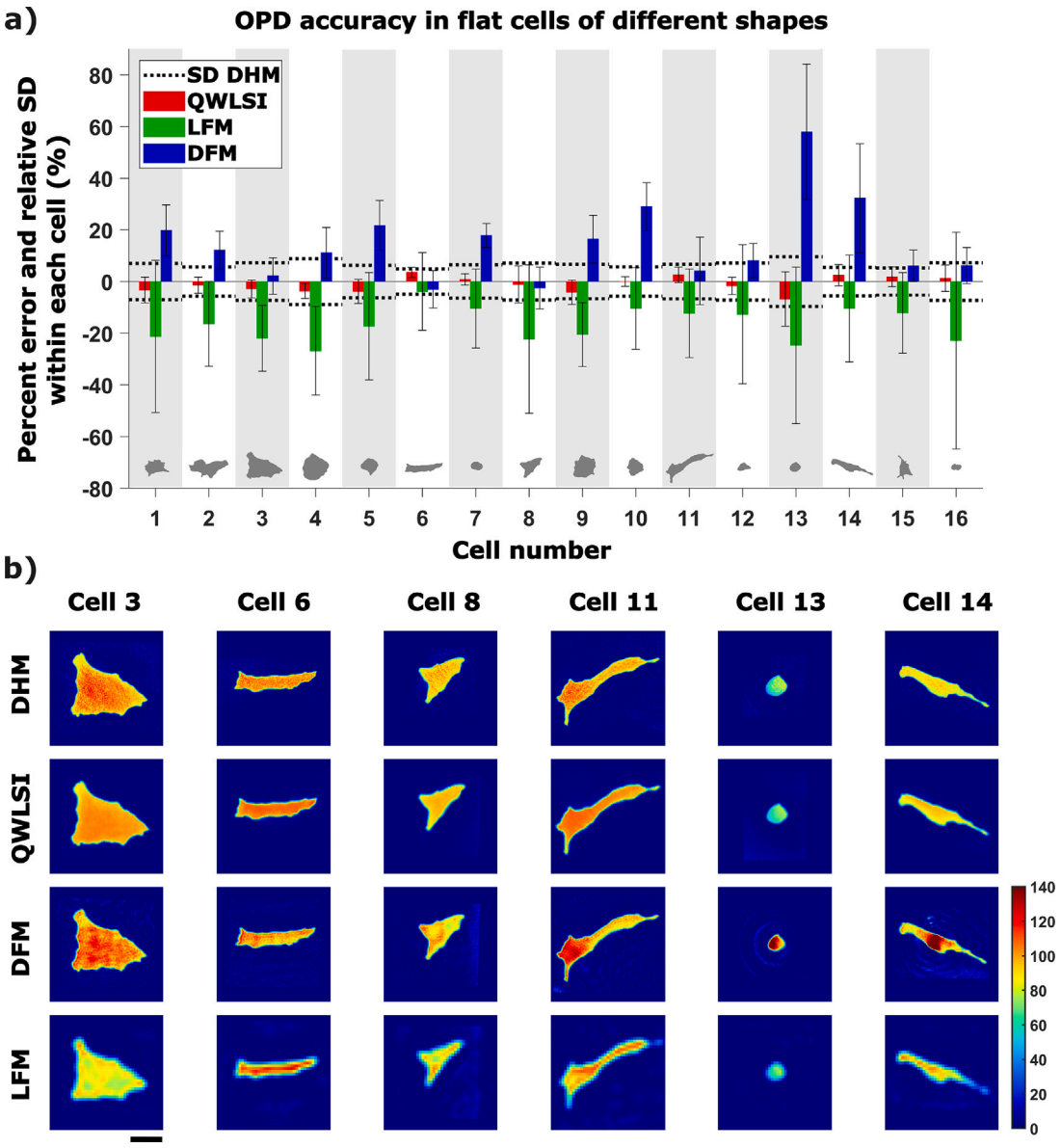

Fig. 2. Results obtained from field 1. (a) Quantitative OPD accuracy analysis with respect to cell shape: bar graph of the percent error PE (relative to DHM measurement) and relative SD for each flat cell. DHM SD is plotted in dashed line. (b) Qualitative comparison of the phase maps of selected cells obtained with each QPI modality. All phase maps are given in supplementary material (Fig. A.2). Scale bar: 20 μm. Color bar: OPD values in nm.

samples, dry mass accuracy and precision can be accessed with respect to height and shape. These conditions were tested using field 3 (consisting of 5 groups of 16 cells with variable height profiles, as defined in Fig. 1(a)). Mean dry mass per field ranges from 61 pg to 512 pg. On the plot of Fig. 4(a), mean PE (data points) and SD (shaded area) were calculated similarly as in field 2, but expressed as dry mass of the cell rather than OPD. The absolute mean PE per group is overall ± 20% or less for all tested modalities. As seen in Fig. 4(a), the zero PE value is reached for a mean dry mass per group of about 200 pg, 300 pg and 400 pg, respectively for QWLSI, LFM and DFM. The dry mass seems generally underestimated for all modalities below this zero PE value and slightly overestimated after it, except for DFM. No critical reconstruction failure was observed at high dry mass values as compared to the results of field 2 at high OPD values, owing to the much lower phase gradients at the edges of the cells. The largest cell mean OPD value in these profiled cells is, however, lower than the largest OPD plateau value in flat cells, with values of 248 nm (with local pixel maxima > 550 nm) vs. 442 nm. The accuracy of the phase results is expected to be higher in field 3 due to the presence of higher frequency components of the OPD (induced by height variations) and the similarity between the training set used for the neural network in LFM and DFM reconstruction and the cells being analyzed.

4. Discussion

This research paves the way to a new gold standard phase-calibration target that can be defined *ad hoc* for different biological applications. The phantom presented here was designed to encompass typical heterogeneity found in adherent cells, in terms of morphological diversity and refractive index ranges, not accessible in standard calibration tools. As an outcome of this study, no clear correlation between cell shape and OPD accuracy was established. Quantitatively, it was shown that measurement errors are generally below or about 10% and 20%, respectively for QWLSI and for DFM and LFM, in flat cells with mean OPD ranging from 100 to 300 nm. With either of the three techniques, a sudden drop in accuracy at higher OPD values is seen. Higher accuracy (PE 10%–15%) is generally achieved in cells with variable height profiles for dry masses of 100 pg and above. This is expected due to

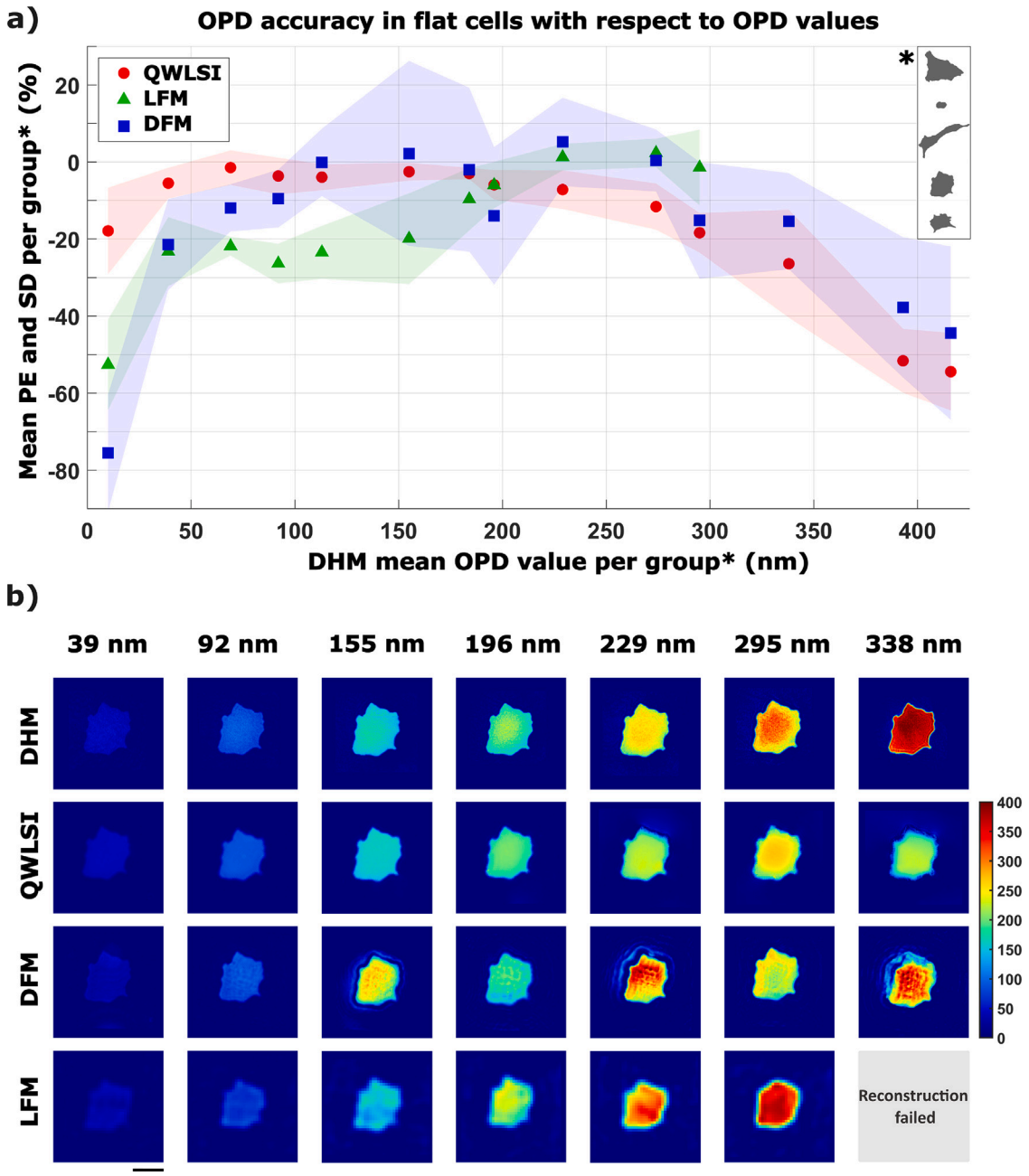

Fig. 3. Results obtained from field 2. (a) OPD accuracy with respect to the OPD value: scatter plot of the mean percent error PE (relative to DHM measurement) and corresponding SD per group (insert *). (b) Phase maps of a single cell at selected OPD values obtained with each QPI modality. Phase maps for all OPD values can be found in the supplementary materials (Fig. A.3). Scale bar: 20 µm. Color bar: OPD values in nm.

the presence of higher frequency components of the OPD (induced by height variations) and the similarity between the training set used for the neural network in LFM and DFM reconstruction and the cells being analyzed.

The phantom may further be used to evaluate repeatability as well as the impact of different imaging protocols on the phase measurements, e.g. changing the focus, the magnification or the phantom position in the FOV (distortion) [15,32]. Software performances can also be investigated to compare different phase reconstruction or segmentation algorithms, especially when combining QPI with machine learning [33–35]. Especially, we decided to manually register the phase maps of the cells to their corresponding shapes of the design maps for direct comparison of the imaging modalities. The shape and area of the cells measured with DHM correspond well to the design, where e.g. thin and elongated features of the cell are retrieved, as shown in the phase maps of supplementary Fig. A.2. We have concluded that the cell masks from design are adequate based on this visual assessment. We have additionally verified that if we expand the cell masks to encompass more area (and thus eventual parts of the cells exceeding the masks), the calculated dry mass increases only by up to 3% in field 3. The cell shape is, however, not always equally preserved in modalities with lower resolution or showing higher field distortion and using a segmentation software instead of the masks may require a further evaluation of the processing algorithm.

Stated accuracy refers to the measurements obtained from the DHM. Alternative methods that are often metrologically traceable and paired with DHM, such as white-light profilometry or atomic force microscopy, could also be used as reference techniques. They, however, only provide height and would require additional measurements in order to provide optical thickness. Designed values should only be used

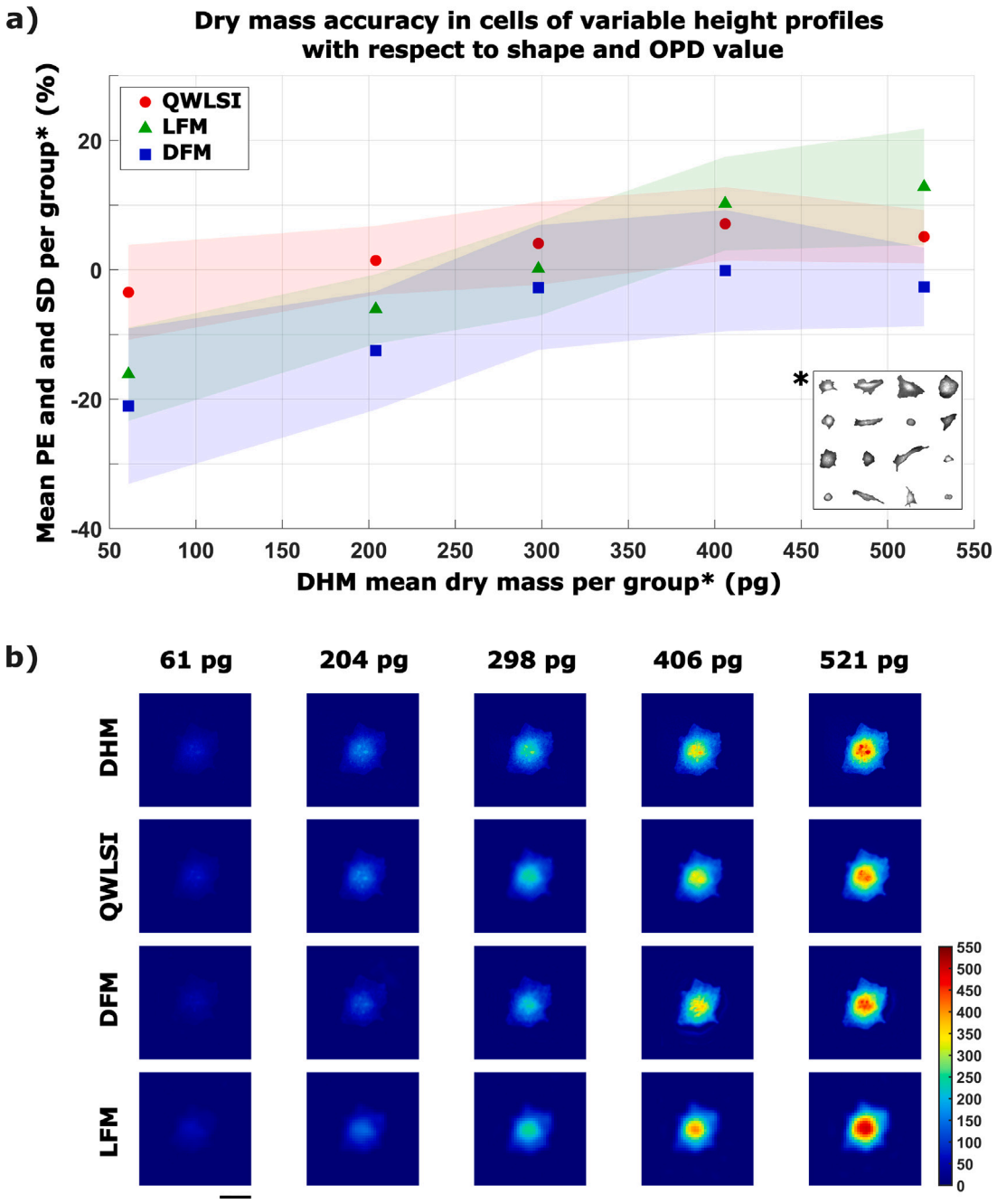

Fig. 4. Results obtained from field 3. (a) Dry mass accuracy with respect to shape and OPD: scatter plot of the mean percent error PE (relative to DHM measurement) and corresponding SD per group (linearly extrapolated in-between subsequent groups). (b) Phase maps of a single cell at different dry mass values obtained with each QPI modality. Scale bar: 20 µm. Color bar: OPD values in nm.

when direct measurements are not feasible, as not all errors introduced by the two-photon polymerization technique can properly be predicted and compensated [36,37]. In such cases, calibration and limitations of the fabrication technique should carefully be evaluated to avoid any bias results. For this phantom, a relatively large printing area was used, resulting in higher deviations from the design at the edges and bottom side of the printed field, as detailed in Methods 5.1.

The flexibility to create a phantom for validating QPI systems in a wide range of measurement scenarios, as well as for isolating individual parameters is a powerful advantage. The phantom design may evolve in the future, with the initial cell phase maps undergoing some adjustments such as scaling (lateral size, phase value) or local density variations. While our study focused on the analysis of individual cells, cell culture features may also be evaluated by changing confluence (e.g. to estimate eventual degradation of the phase measurement at large cell population density) or merging cells from various dishes (e.g. different cell types or experimental conditions). Free-floating cell phantoms could also be fabricated using this approach to accommodate QPI imaging of cells in suspension (e.g. non-adherent, flow cytometry). For example, the phantoms could be released from the substrate when coated with a sacrificial layer (such as polyvinyl alcohol) that is dissolvable in water. Another approach is to fabricate detached cells directly in the microfluidic channel at high printing speed, so that any displacement errors during printing are minimized. Compared to common phase calibration tools, e.g. polystyrene beads, our 3D printed phantoms give a more realistic representation of various biological samples. While they may appear beyond reach for some users, in terms of access to printing facilities and fabrication costs, different

approaches may be considered to overcome these issues. On one side, printing-on-demand services may accommodate fabrication of such phantom design. On the other side, the fabrication cost per piece may dramatically be lowered using molding and replication techniques [38].

Using such phantom, experimental protocols and post-processing pipelines can therefore be refined by tuning the appropriate parameters in order to maximize accuracy and precision prior to any large scale biological study. The scope of applications and limitations can methodologically be defined, which is essential to exclude potential sources of errors. This way, it may help opening up novel directions on the use of QPI methodologies to identify fluctuations at different order of magnitudes and decipher the interplay between cellular features and their cell cycle regulation [12]. Finally, it can enhance inter-laboratories comparison where the same 3D printed phantom can be imaged with multiple set-ups as in this study, providing it can easily be transferred between facilities. Thereby, it may strengthen the validity of new results, providing a common reference when addressing a particular biological question, pointing out reasons between eventual disparities in reproducibility and replicability studies and establishing best practises.

5. Methods

5.1. Phantom fabrication

The fabrication was performed using two-photon polymerization lithography [39] system (Photonic Professional GT2, Nanoscribe GmbH & Co. KG, Germany). In short, tightly focused femtosecond laser beam induces local polymerization of the photosensitive resin. By scanning the focus across the resin in line-by-line and layer-by-layer fashion it is possible to 3D-print transparent microstructures with submicrometer resolution. This approach enables fabrication on top of microscopy slide, coverslip or inside Petri micro-dish, which it is compatible with most QPI systems. In order to define the phantom in terms of height profile required for the lithography system, the phase map (ϕ) has been converted to height map (h) using the following relationship: $h = \lambda\phi/(2\pi\Delta RI)$, where λ is the wavelength of light and ΔRI refers to the refractive index difference between the fabricated structures and the surrounding medium. In this case the targeted was $\Delta RI = 0.038$ and $\lambda = 632\,\text{nm}$. In terms of the fabrication accuracy, the electron microscopy images confirmed the lateral size of the features at the order of 100 nm (Fig. 1b). In terms of OPD accuracy, we have noticed 5%–50% error when compared to the designed OPD as shown in supplementary Fig. A.4, most likely due to the anisotropic shrinkage (depending on the cell shape and height), as well as variable energy dose of the polymerization beam that depends on the location of the cell within the printed field of view [38–41]. Higher variations (> 30 %) are obtained in the bottom row of cells for all printed fields while the error is usually lower in centered and upper cells (<15% for flat cells and <20% for cells with variable height profiles), likely due to the imperfect adjustments of the galvo scanners. For this reason, the evaluation is performed relative to the best available QPI system, as it is robust against any fabrication errors that could occur. Sample roughness for this printing setup is estimated at 10–50 nm. Even at the worst case of 50 nm, it is equivalent to 1.9 nm OPD at 0.038 refractive index contrast, which is below practical considerations and lower than the measured precision, which is 4 nm OPD at its minimum (and on average 6 nm OPD from the data in Fig. 2).

The designed phantom has been fabricated on top of the 25 × 25 × 0.7 mm fused silica substrate, immersed in Immersol 518F (Carl Zeiss AG, Germany) and covered with a 24 × 60 × 0.17 mm coverslip with a 80 μm spacer inbetween.

5.2. QPI systems, measurements and reconstruction

5.2.1. Digital holographic microscope

The DHM results were captured using a Mach–Zehnder-based microscope (Fig. 5d) capable of angular scanning of the illumination beam, essentially performing an optical diffraction tomography reconstruction. This approach enables measurements of phase maps with superior accuracy, spatial resolution, signal-to-noise and extended depth of field when compared to the standard DHM [42]. The 633 nm wavelength single longitudinal mode laser beam (Necsel/Ushio, USA) is delivered with an optical fiber, collimated and then split into object and reference arm. The object beam is steered with a dual-axis MEMS mirror (Mirrorcle Technologies Inc., USA) into the illumination 4f system (custom 140 mm tube lens and NA 1.0, 40x water objective), passes through the sample and is captured by another 4f system that relays the object's plane to the camera plane (NA 1.3 oil immersion imaging objective and 200 mm tube lens). The beams recombine at a slight angle forming an off-axis hologram recorded by the 2/3" CMOS camera with a pixel of 3.45 μm (JAI). A single tomographic acquisition comprise of 91 holograms, 90 of which are captured at the angle near the maximal NA (zenith angle $\theta = 30°$) forming a circular pattern at the back focal plane of the objective. One additional image is captured for the axial object beam as in typical DHMs. Complex amplitude of each hologram is retrieved using Fourier transform method [43]. Optical aberrations and systematic errors are compensated using the measurement with no objects visible in the measurement volume. Finally, the phase maps are obtained from the reconstructed 3D refractive index distribution by integrating phase delays resulting from the refractive index variations within the sample volume. The phase map retrieved this way is best described as "integrated phase", and it features numerous advantages compared to the regular DHM or any other QPI system in general:

- High accuracy of the phase on individual projections, since the OPD is compared directly to the accurate and precise wavelength [44];
- high lateral resolution (~150 nm half-pitch) owing to high-NA of both objectives and synthesized objects' frequencies via diffraction tomography reconstruction [45];
- improved precision and signal-to-noise due to the synthetic aperture and averaging of multiple projections;
- minimized diffraction artifacts from objects being out-of-focus or exceeding the depth of field, since the final phase is obtained from the refractive index distribution by integrating phase delays introduced by each voxel along the Z (axial) direction ($\Delta\phi = 2\pi\Delta z\Delta RI/\lambda$).

5.2.2. Quadri-wave lateral shearing interferometer

QWLSI (Fig. 5c) was performed on a home-built inverted microscope, with a 0.35 NA air objective (Olympus SLMPLN50X) matched with a 100 mm focal length achromatic doublet (Thorlabs AC254-100-A-ML), yielding an optical magnification of 27.78. Kohler-type illumination at 530 nm is used, fed by a LED (Thorlabs M530L4) through a multi-mode 1500 μm diameter core, 0.39 NA optical fiber (Thorlabs M93L01). The interferometry was performed on a SID4-sC8 wavefront sensor (Phasics SA, Saint-Aubin, France) mounted as a camera on the microscope: the wavefront sensor contains a 2D grating (modified Hartmann mask) placed in front of a sCMOS sensor. The grating replicates the incident wavefront and an interferogram is recorded on the sensor. The interferogram is analyzed in real time by Fourier transforms to extract (*i*) an intensity image at order 0 and (*ii*) phase gradients along X and Y at order 1. Through a proprietary API provided by the manufacturer, these gradients are integrated in two dimensions to yield a wavefront measurement, which corresponds to an OPD image in the projective approximation [28]. The intensity and phase images obtained have effective pixel pitches of 19.5 μm on the sensor plane, due to a necessary 2x2 binning with respect to the physical pixels,

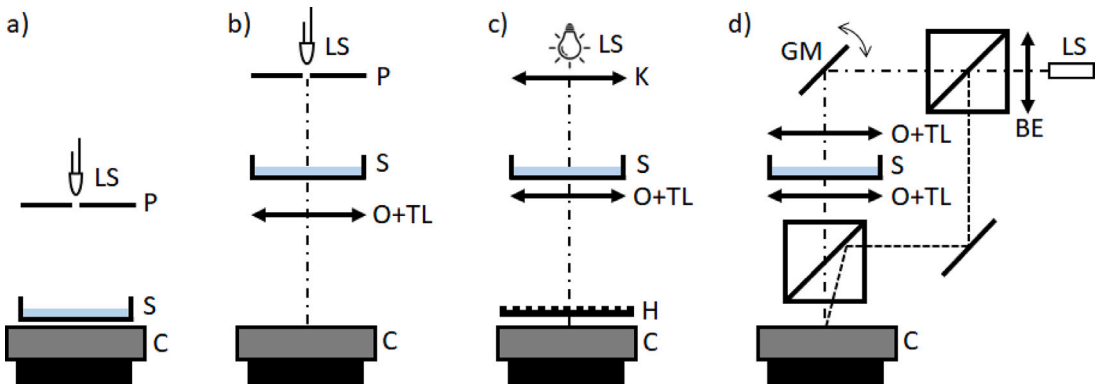

Fig. 5. QPI systems: (a) lensfree microscope (LFM), (b) defocused microscope (DFM), (c) quadri-wave lateral shearing interferometer (QWLSI), (d) digital holographic microscope (DHM). LS — light source, S — sample, C — camera, P — pinhole, O+TL — objective with tube lens, K — Köhler illumination, H — modified Hartmann mask, GM — galvanometric mirrors, BE — beam expander.

corresponding to 0.702 µm/pixel in the object plane.

This imaging technique requires the sample to be in-focus. The focus position is adjusted using a piezoelectric stage after performing an autofocusing sequence, as described in the next Section 5.2.3. It also requires a reference image, to be taken in conditions as close as possible to the imaging conditions of the sample, but without a sample. It was recorded on an background area of the sample (i.e with no printed pattern) and with the same illumination and exposure conditions as used for the sample measurements. A unique reference measurement was used for the whole sample.

5.2.3. Defocused microscope

DF imaging (Fig. 5b) was performed on a home-built inverted microscope, with a 0.25 NA air objective (Olympus PLN10X) matched with a 100 mm focal length achromatic doublet (Thorlabs AC254-100-A-ML), yielding an optical magnification of 5.56. Illumination was provided by the blue channel of a OSRAM LZ4-60MD09 RGBW LED emitter, through a 40° diffuser and a 400 µm pinhole, and spectrally filtered at 450 nm with 10 nm FWHM (Edmund Optics 34499). The images were captured on a monochrome CMOS sensor with 2.4 µm pixel pitch (IDS U3-3880SE-M-GL), corresponding to 0.432 µm/pixel in the object plane. They were recorded with a defocus of −150 µm, i.e with an object focal plane 150 µm away from the sample plane, in the direction of the source. To repeatably achieve the same defocus, an autofocusing sequence was used to detect the sample plane and then the microscope objective was moved 150 µm in the direction of the light source (upwards in our setup) by a piezoelectric stage. The autofocus sequence consists in taking a stack of 31 images, one every 10 µm using the piezoelectric stage holding the microscope objective, computing the standard deviation of pixel values for each image and interpolating the stage position for which this value is minimal. The calculated focus values were visually checked with the recordings of in-focus bright-field images. Image reconstruction for DFM and LFM imaging is similar and detailed in the next section.

5.2.4. Lensfree microscope

LF imaging (Fig. 5a) was performed using a home-built system consisting of an OSRAM LZ4-60MD09 RGBW LED emitter through a 40° diffuser and 50 µm pinhole, and a monochrome 1.67 µm pixel pitch CMOS sensor (IDS UI-1492LE). The illumination wavelengths (blue, green, red) are centered around 450 , 540 and 630 nm, respectively. Red, green and blue-illuminated images were recorded sequentially with the respective light intensities of each color adjusted such that the average pixel value was comparable across all channels. The CMOS sensor was placed as close as possible to the microscope slide holding the sensor, while still avoiding any mechanical conflict with the sample holder (Thorlabs MLS203P10) and the motorized XY-translation stage holding it (Thorlabs MLS203-1). This resulted in a sample to sensor distance of approximately 1.7 mm.

Images acquires with the LFM and DFM were reconstructed using an updated version of the algorithm described in [34]. The reconstruction process involves alternating between two approaches, an inverse problem optimization and deep learning. The optimization starts with several iterations of a conventional gradient descent optimization algorithm, resulting in a preliminary estimate of the cell sample image. This image is then passed into a neural network, previously trained on simulation data. The neural network aids in reducing phase wrapping errors and enhances resolution, particularly in cases of high cell density. The predicted image serves as the initialization of a second and final reconstruction step, which corrects to a certain extent the neural network prediction errors. In this study, we used a more powerful neural network, namely the UneXt [46], and more sophisticated training procedure. We also significantly increase the quality of the simulation dataset by introducing more variation in cell shapes and their spatial organization, rendering the scene more realistic.

5.3. Processing pipeline and quantified parameters

The processing pipeline (Fig. 6) has been designed to prioritize accuracy and repeatability of the individual cell measurement results and enable direct comparison of all systems. The following steps are:

- Resampling and alignment: the magnification of all systems has been determined on the calibration lines fabricated alongside the cell phantoms. The expected (designed) phase maps used for the fabrication have been resampled to match the pixel size of each system, and then rotated in order to align their coordinate systems. In both steps linear interpolation method was used. We specifically avoided resampling and rotating the original phase maps in order to minimize interpolation artifacts on noisy experimental data.
- Cell registration and segmentation: individual cells have been manually cropped and registered to their corresponding shapes of the designed phase map, which would be equivalent to the perfect segmentation algorithm. Two segmented regions are: cell (within the red outline) and background (green area; 3 µm thick and distanced 3 µm away from the cell boundary).
- Phase correction: first, the phase tilt and offset have been compensated with high accuracy using the background region segmented in the previous step. Then, the phase differences related to the refractive index dispersion have been compensated using the β factor, enabling direct comparison of the phase despite all systems using different illumination wavelengths.

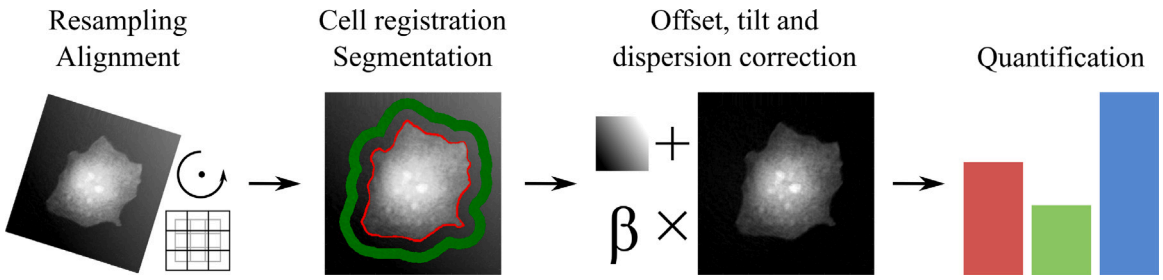

Fig. 6. Processing pipeline enabling direct comparison of the results from all systems. See text for details.

- Quantification of key parameters: In the flat cells of fields 1 and 2, OPD (in nm) in each (x,y) position of the cell is retrieved, after erosion of 3 μm from the cell boundary (large phase gradients at the edge of cells):

$$OPD(x,y) = \lambda \frac{\Delta\phi(x,y)}{2\pi} = \int_0^h \Delta RI(x,y,z)\,dz \tag{1}$$

where λ is the illumination wavelength, $\Delta\phi$ and ΔRI the phase and refractive index difference between sample and surrounding medium, respectively, and h the sample height.
In the cells of variable height profiles of field 3, dry mass DM (in pg) is obtained after integration of the OPD values over the entire projected area (without erosion):

$$DM(x,y) = \frac{1}{\alpha}\int_S OPD(x,y)\,dx dy \tag{2}$$

where $\alpha = 0.18\ \mu m^3\ pg^{-1}$ is the specific refractive index increment for cells in water [19]. Using this value, as it is unknown for the polymer, dry mass should rather be considered as 'dry mass equivalent'.

5.4. Metrics for accuracy and precision analysis

Accuracy and precision of the quantified parameters in the whole cells have been investigated. However, in principle, any other feature vector that is advantageous for another particular application can be used.

For field 1, OPD accuracy for each cell was assessed via the percent error:

$$PE\ (\%) = \frac{\mu(OPD_{sys}) - \mu(OPD_{DHM})}{\mu(OPD_{DHM})} * 100 \tag{3}$$

where μ is the mean OPD value per cell retrieved for each modality (ground truth DHM, sys= LFM, DFM or QWLSI).

In addition, the relative standard deviation per cell is calculated to estimate the precision of the measurements and its variations depending on the cell shape:

$$RSD\ (\%) = \frac{\sigma(OPD_{sys})}{\mu(OPD_{sys})} * 100 \tag{4}$$

where σ is the SD value per cell per modality.

For field 2, the PE per cell is obtained as for field 1 before computing the mean PE per group (average of 5 cells) and its corresponding SD, to access accuracy and precision, respectively, on the entire group (instead of on individual cell as in field 1). For field 3, mean PE and SD per group (average of 16 cells) were calculated similarly as in field 2, using dry mass instead of OPD as a parameter in Eq. (3).

CRediT authorship contribution statement

Sylvia Desissaire: Writing – original draft, Visualization, Methodology, Investigation, Formal analysis, Data curation, Conceptualization. **Michał Ziemczonok:** Writing – original draft, Visualization, Methodology, Investigation, Data curation, Conceptualization. **Tigrane Cantat-Moltrecht:** Writing – original draft, Methodology, Investigation. **Arkadiusz Kuś:** Writing – review & editing, Software, Conceptualization. **Guillaume Godefroy:** Writing – original draft, Software. **Lionel Hervé:** Writing – review & editing, Software. **Chiara Paviolo:** Writing – original draft, Project administration, Funding acquisition. **Wojciech Krauze:** Writing – review & editing, Project administration, Methodology, Funding acquisition, Conceptualization. **Cédric Allier:** Writing – review & editing, Methodology, Investigation, Conceptualization. **Ondrej Mandula:** Writing – review & editing, Visualization, Investigation, Conceptualization. **Małgorzata Kujawińska:** Writing – review & editing, Project administration, Funding acquisition.

Declaration of competing interest

The authors declare that they have no known competing financial interests or personal relationships that could have appeared to influence the work reported in this paper.

Acknowledgments

This work has received funding from the European Union's Horizon 2020 research program under grant agreement N° 101016726. This work has also been funded in part by the Polish Ministry of Education and Science (Polish Metrology, PM/SP/0079/2021/1) and Warsaw University of Technology, Poland under the program Excellence Initiative: Research University (IDUB). MZ acknowledges the support by the Foundation for Polish Science (FNP).

Appendix A. Supplementary material

Supplementary material related to this article can be found online at https://doi.org/10.1016/j.measurement.2025.116765.

Data availability

Data will be made available on request.

References

[1] Y. Park, C. Depeursinge, G. Popescu, Quantitative phase imaging in biomedicine, Nat. Photon 12 (10) (2018) 578–589, http://dx.doi.org/10.1038/s41566-018-0253-x.

[2] F. Zernike, Das phasenkontrastverfahren bei der mikroskopischen beobachtung, Z. Tech. Phys. 16 (11) (1935) 454–457.

[3] V. Balasubramani, M.g. Kujawińska, C. Allier, V. Anand, C.-J. Cheng, C. Depeursinge, N. Hai, S. Juodkazis, J. Kalkman, A. Kuś, M. Lee, P.J. Magistretti, P. Marquet, S.H. Ng, J. Rosen, Y.K. Park, M. Ziemczonok, Roadmap on digital holography-based quantitative phase imaging, J. Imaging 7 (12) (2021) 252, http://dx.doi.org/10.3390/jimaging7120252.

[4] G. Popescu, Y. Park, N. Lue, C. Best-Popescu, L. Deflores, R.R. Dasari, M.S. Feld, K. Badizadegan, Optical imaging of cell mass and growth dynamics, Am. J. Physiol. Cell Physiol. 295 (2) (2008) C538–544, http://dx.doi.org/10.1152/ajpcell.00121.2008.

[5] M. Mir, Z. Wang, Z. Shen, M. Bednarz, R. Bashir, I. Golding, S.G. Prasanth, G. Popescu, Optical measurement of cycle-dependent cell growth, Proc. Natl. Acad. Sci. USA 108 (32) (2011) 13124–13129, http://dx.doi.org/10.1073/pnas.1100506108.

[6] K.L. Cooper, S. Oh, Y. Sung, R.R. Dasari, M.W. Kirschner, C.J. Tabin, Multiple phases of chondrocyte enlargement underlie differences in skeletal proportions, Nature 495 (7441) (2013) 375–378, http://dx.doi.org/10.1038/nature11940.

[7] W.J. Eldridge, S. Ceballos, T. Shah, H.S. Park, Z.A. Steelman, S. Zauscher, A. Wax, Shear modulus measurement by quantitative phase imaging and correlation with atomic force microscopy, Biophys. J. 117 (4) (2019) 696–705, http://dx.doi.org/10.1016/j.bpj.2019.07.008.

[8] Z.A. Steelman, Z.N. Coker, A. Kiester, G. Noojin, B.L. Ibey, J.N. Bixler, Quantitative phase microscopy monitors subcellular dynamics in single cells exposed to nanosecond pulsed electric fields, J. Biophotonics 14 (10) (2021) e202100125, http://dx.doi.org/10.1002/jbio.202100125.

[9] Y. Zhang, R.L. Judson, Evaluation of holographic imaging cytometer holomonitor M4® motility applications, Cytom. A 93 (11) (2018) 1125–1131, http://dx.doi.org/10.1002/cyto.a.23635.

[10] Y. Li, J. Di, W. Wu, P. Shang, J. Zhao, Quantitative investigation on morphology and intracellular transport dynamics of migrating cells, Appl. Opt. 58 (34) (2019) G162–G168, http://dx.doi.org/10.1364/AO.58.00G162.

[11] L. Ghenim, C. Allier, P. Obeid, L. Hervé, J.-Y. Fortin, M. Balakirev, X. Gidrol, A new ultradian rhythm in mammalian cell dry mass observed by holography, Sci. Rep. 11 (1) (2021) 1290, http://dx.doi.org/10.1038/s41598-020-79661-9.

[12] X. Liu, S. Oh, L. Peshkin, M.W. Kirschner, Computationally enhanced quantitative phase microscopy reveals autonomous oscillations in mammalian cell growth, Proc. Natl. Acad. Sci. USA 117 (44) (2020) 27388–27399, http://dx.doi.org/10.1073/pnas.2002152117.

[13] C. Allier, L. Hervé, O. Mandula, P. Blandin, Y. Usson, J. Savatier, S. Monneret, S. Morales, Quantitative phase imaging of adherent mammalian cells: a comparative study, Biomed. Opt. Express, BOE 10 (6) (2019) 2768–2783, http://dx.doi.org/10.1364/BOE.10.002768.

[14] A. Ahmad, V. Dubey, A. Butola, B.S. Ahluwalia, D.S. Mehta, Highly temporal stable, wavelength-independent, and scalable field-of-view common-path quantitative phase microscope, JBO 25 (11) (2020) 116501, http://dx.doi.org/10.1117/1.JBO.25.11.116501.

[15] T.L. Nguyen, S. Pradeep, R.L. Judson-Torres, J. Reed, M.A. Teitell, T.A. Zangle, Quantitative phase imaging: Recent advances and expanding potential in biomedicine, ACS Nano 16 (8) (2022) 11516–11544, http://dx.doi.org/10.1021/acsnano.1c11507.

[16] R. Horstmeyer, R. Heintzmann, G. Popescu, L. Waller, C. Yang, Standardizing the resolution claims for coherent microscopy, Nat. Photonics 10 (2) (2016) 68–71, http://dx.doi.org/10.1038/nphoton.2015.279.

[17] T.M. Godden, A. Muñiz-Piniella, J.D. Claverley, A. Yacoot, M.J. Humphry, Phase calibration target for quantitative phase imaging with ptychography, Opt. Express 24 (7) (2016) 7679–7692, http://dx.doi.org/10.1364/OE.24.007679.

[18] Z. Wang, D.L. Marks, P.S. Carney, L.J. Millet, M.U. Gillette, A. Mihi, P.V. Braun, Z. Shen, S.G. Prasanth, G. Popescu, Spatial light interference tomography (SLIT), Opt. Express 19 (21) (2011) 19907–19918, http://dx.doi.org/10.1364/OE.19.019907.

[19] R. Barer, Interference microscopy and mass determination, Nature 169 (4296) (1952) 366–367, http://dx.doi.org/10.1038/169366b0.

[20] B. Rappaz, A. Barbul, Y. Emery, R. Korenstein, C. Depeursinge, P.J. Magistretti, P. Marquet, Comparative study of human erythrocytes by digital holographic microscopy, confocal microscopy, and impedance volume analyzer, Cytom. Part A 73A (10) (2008) 895–903, http://dx.doi.org/10.1002/cyto.a.20605.

[21] J. Reed, J. Chun, T.A. Zangle, S. Kalim, J.S. Hong, S.E. Pefley, X. Zheng, J.K. Gimzewski, M.A. Teitell, Rapid, massively parallel single-cell drug response measurements via live cell interferometry, Biophys. J. 101 (5) (2011) 1025–1031, http://dx.doi.org/10.1016/j.bpj.2011.07.022.

[22] K. Wang, C.-C. Ho, C. Zhang, B. Wang, A review on the 3D printing of functional structures for medical phantoms and regenerated tissue and organ applications, Engineering 3 (5) (2017) 653–662, http://dx.doi.org/10.1016/J.ENG.2017.05.013.

[23] V. Filippou, C. Tsoumpas, Recent advances on the development of phantoms using 3D printing for imaging with CT, MRI, PET, SPECT, and ultrasound, Med. Phys. 45 (9) (2018) e740–e760, http://dx.doi.org/10.1002/mp.13058.

[24] M. Eifler, J. Hering, J. Seewig, R.K. Leach, G. von Freymann, X. Hu, G. Dai, Comparison of material measures for areal surface topography measuring instrument calibration, Surf. Topography: Metrol. Prop. 8 (2) (2020) 025019, http://dx.doi.org/10.1088/2051-672X/ab92ae.

[25] G. Veres, J. Kiss, N.F. Vas, P. Kallos-Balogh, N.B. Máthé, M.L. Lassen, E. Berényi, L. Balkay, Phantom study on the robustness of MR radiomics features: Comparing the applicability of 3D printed and biological phantoms, Diagnostics 12 (9) (2022) 2196, http://dx.doi.org/10.3390/diagnostics12092196.

[26] M. Woletz, F. Chalupa-Gantner, B. Hager, A. Ricke, S. Mohammadi, S. Binder, S. Baudis, A. Ovsianikov, C. Windischberger, Z. Nagy, Toward printing the brain: A microstructural ground truth phantom for MRI, Adv. Mater. Technol. 9 (3) (2024) 1–9, http://dx.doi.org/10.1002/admt.202300176.

[27] M. Ziemczonok, A. Kuś, P. Wasylczyk, M. Kujawińska, 3D-printed biological cell phantom for testing 3D quantitative phase imaging systems, Sci. Rep. 9 (1) (2019) 18872, http://dx.doi.org/10.1038/s41598-019-55330-4.

[28] P. Bon, G. Maucort, B. Wattellier, S. Monneret, Quadriwave lateral shearing interferometry for quantitative phase microscopy of living cells, Opt. Express, OE 17 (15) (2009) 13080–13094, http://dx.doi.org/10.1364/OE.17.013080.

[29] S.V. Kesavan, F. Momey, O. Cioni, B. David-Watine, N. Dubrulle, S. Shorte, E. Sulpice, D. Freida, B. Chalmond, J.M. Dinten, X. Gidrol, C. Allier, High-throughput monitoring of major cell functions by means of lensfree video microscopy, Sci Rep 4 (1) (2014) 5942, http://dx.doi.org/10.1038/srep05942.

[30] O. Mandula, J.-P. Kleman, F. Lacroix, C. Allier, D. Fiole, L. Hervé, P. Blandin, D.C. Kraemer, S. Morales, Phase and fluorescence imaging with a surprisingly simple microscope based on chromatic aberration, Opt. Express, OE 28 (2) (2020) 2079–2090, http://dx.doi.org/10.1364/OE.28.002079.

[31] P. Llopis, R. Senft, T. Ross-Elliott, R. Stephansky, D. Keeley, P. Koshar, G. Marqués, Y.-s. Gao, B. Carlson, T. Pengo, M. Sanders, L. Cameron, M. Itano, Best practices and tools for reporting reproducible fluorescence microscopy methods, Nature Methods 18 (12) (2021) 1463–1476, http://dx.doi.org/10.1038/s41592-021-01156-w.

[32] S. Aknoun, J. Savatier, P. Bon, F. Galland, L. Abdeladim, B. Wattellier, S. Monneret, Living cell dry mass measurement using quantitative phase imaging with quadriwave lateral shearing interferometry: An accuracy and sensitivity discussion, J. Biomed. Opt. 20 (12) (2015) 126009, http://dx.doi.org/10.1117/1.JBO.20.12.126009.

[33] Y. Jo, H. Cho, S.Y. Lee, G. Choi, G. Kim, H.-s. Min, Y. Park, Quantitative phase imaging and artificial intelligence: A review, IEEE J. Sel. Top. Quantum Electron. 25 (1) (2019) 1–14, http://dx.doi.org/10.1109/JSTQE.2018.2859234.

[34] L. Hervé, D. Kraemer, O. Cioni, O. Mandula, M. Menneteau, S. Morales, C. Allier, Alternation of inverse problem approach and deep learning for lens-free microscopy image reconstruction, Sci. Rep. 10 (1) (2020) 20207, http://dx.doi.org/10.1038/s41598-020-76411-9.

[35] C. Allier, L. Hervé, C. Paviolo, O. Mandula, O. Cioni, W. Pierré, F. Andriani, K. Padmanabhan, S. Morales, CNN-Based cell analysis: From image to quantitative representation, Front. Phys. 9 (2022) http://dx.doi.org/10.3389/fphy.2021.776805.

[36] X. Zhou, Y. Hou, J. Lin, A review on the processing accuracy of two-photon polymerization, AIP Adv. 5 (3) (2015) 030701, http://dx.doi.org/10.1063/1.4916886.

[37] F. Cantoni, D. Maher, E. Bosler, S. Kühne, L. Barbe, D. Oberschmidt, C. Marquette, R. Taboryski, M. Tenje, A.-I. Bunea, Round-robin testing of commercial two-photon polymerization 3D printers, Addit. Manuf. 76 (2023) 103761, http://dx.doi.org/10.1016/j.addma.2023.103761.

[38] H. Wang, C.-F. Pan, C. Li, K.S. Menghrajani, M.A. Schmidt, A. Li, F. Fan, Y. Zhou, W. Zhang, H. Wang, P.N.S. Nair, J.Y.E. Chan, T. Mori, Y. Hu, G. Hu, S.A. Maier, H. Ren, H. Duan, J.K.W. Yang, Two-photon polymerization lithography for imaging optics, Int. J. Extrem. Manuf. 6 (4) (2024) 042002, http://dx.doi.org/10.1088/2631-7990/ad35fe.

[39] H. Wang, W. Zhang, D. Ladika, H. Yu, D. Gailevičius, H. Wang, C.-F. Pan, P.N.S. Nair, Y. Ke, T. Mori, J.Y.E. Chan, Q. Ruan, M. Farsari, M. Malinauskas, S. Juodkazis, M. Gu, J.K.W. Yang, Two-photon polymerization lithography for optics and photonics: Fundamentals, materials, technologies, and applications, Adv. Funct. Mater. 33 (39) (2023) 2214211, http://dx.doi.org/10.1002/adfm.202214211.

[40] H. Wang, H. Wang, Q. Ruan, J.Y.E. Chan, W. Zhang, H. Liu, S.D. Rezaei, J. Trisno, C.-W. Qiu, M. Gu, J.K.W. Yang, Coloured vortex beams with incoherent white light illumination, Nature Nanotechnology 18 (3) (2023) 264–272, http://dx.doi.org/10.1038/s41565-023-01319-0.

[41] H. Wang, H. Wang, Q. Ruan, Y.S. Tan, C.-W. Qiu, J.K.W. Yang, Optical fireworks based on multifocal three-dimensional color prints, ACS Nano 15 (6) (2021) 10185–10193, http://dx.doi.org/10.1021/acsnano.1c02131.

[42] Y. Cotte, F. Toy, P. Jourdain, N. Pavillon, D. Boss, P. Magistretti, P. Marquet, C. Depeursinge, Marker-free phase nanoscopy, Nat. Photonics 7 (2) (2013) 113–117, http://dx.doi.org/10.1038/nphoton.2012.329.

[43] A. Kuś, W. Krauze, P.L. Makowski, M. Kujawińska, Holographic tomography: hardware and software solutions for 3D quantitative biomedical imaging, ETRI J. 41 (1) (2019) 61–72, http://dx.doi.org/10.4218/etrij.2018-0505.

[44] Y. Emery, T. Colomb, E. Cuche, Metrology applications using off-axis digital holography microscopy, J. Phys.: Photonics 3 (3) (2021) 034016, http://dx.doi.org/10.1088/2515-7647/ac0957.

[45] N. Verrier, M. Debailleul, O. Haeberlé, Recent advances and current trends in transmission tomographic diffraction microscopy, Sensors 24 (5) (2024) 1594, http://dx.doi.org/10.3390/s24051594.

[46] J.M.J. Valanarasu, V.M. Patel, UNeXt: MLP-based rapid medical image segmentation network, in: Medical Image Computing and Computer Assisted Intervention – MICCAI 2022, vol. 13435, Springer Nature Switzerland, 2022, pp. 23–33, http://dx.doi.org/10.1007/978-3-031-16443-9_3.